Original Article

Metal artifact reduction using mono-energy images combined with metal artifact reduction software in spectral computed tomography: a study on phantoms

Xiaoli Sun, Qingqing Zhao, Pengtao Sun, Zhipeng Yao, Rengui Wang

Department of Radiology, Beijing Shijitan Hospital, Peking University Ninth School of Clinical Medicine, Capital Medical University, Beijing, China

Correspondence to: Rengui Wang. Department of Radiology, Beijing Shijitan Hospital, Peking University Ninth School of Clinical Medicine, Capital Medical University, Beijing, China. Email: 490150302@qq.com.

Background: This study aimed to evaluate the effectiveness of spectral computed tomography (CT) mono-energy imaging combined with metal artifact reduction software (MARs) for metal implant artifact reduction using a phantom.

Methods: A quantitative standard phantom with 9 cylinders was used to simulate the attenuation of the different tissues of the human body around the metal implant. Groups A and B were divided according to conventional CT scan mode and spectral CT scan mode. Three sets of reconstructed images, including 120 kVp-like + MARs images, mono-energy images (MonoE), and MonoE + MARs images, were generated after spectral CT scanning. High-attenuation artifacts and low-attenuation artifacts were observed around the coil in the images of groups A and B. The CT values (Hounsfield unit) and standard deviation (SD) values of the artifacts were measured, and the artifact index and hardening artifact removal rate were calculated.

Results: Compared to conventional poly-energy CT images, for high-attenuation and low-attenuation artifacts, the artifact indices of 120 kVp-like + MARs, MonoE, and MonoE + MARs images were all reduced significantly. The hardening artifact removal rates of the high-attenuation and low-attenuation artifacts of 120 kVp-like + MARs images were 82% and 92%, respectively. The hardening artifact removal rate of the high-attenuation and low-attenuation artifacts of MonoE and MonoE + MARs images increased with the mono-energy level.

Conclusions: Spectral CT using the 120 kVp-like + MARs, 110–140 keV MonoE, and MonoE + MARs reconstruction methods can reduce metal implant artifacts in varying degrees. MonoE + MARs reconstruction was the best method for reducing metal artifacts.

Keywords: Special CT; metal artifact reduction software (MARs); mono-energy imaging; metal implant artifacts

Submitted Nov 09, 2019. Accepted for publication Jun 17, 2020.
doi: 10.21037/qims-19-936
View this article at: http://dx.doi.org/10.21037/qims-19-936

Introduction

Cirrhosis is a common chronic liver disease in China. The portal blood flow rate is increasingly resisted in patients with cirrhosis, thus causing portal hypertension. Esophageal varices bleeding (EVB) is the most dangerous complication of portal hypertension. Transjugular intrahepatic portosystemic shunt (TIPS) combined with gastric coronary vein embolization (GCVE) is one of the most important and effective treatments for EVB (1,2). A CT scan is a vital follow-up method for evaluating the effect of TIPS combined with GCVE. It is well-known that the detachable metallic coil used in GCVE causes dark and bright streaks that impair the image quality of the surrounding tissues (3-6).

Different approaches for metal artifact reduction (MAR)

have been described, including physical prefiltering, calibration correction, and dual-energy scanning. Many post-processing algorithms for MAR have been reported (7-11). Some recent studies have indicated that MAR and dual-energy CT hold advantages for reducing metal artifacts from bipolar hemiarthroplasty and total hip arthroplasty phantoms, total hip replacements, and intracranial clips and coils (12-14). Given that MAR can be applied to all mono-energy CT scans, MAR combined with a mono-energy CT could further improve the capabilities of the individual technique alone. However, the shape, size, and type of metal used in the studies mentioned above are different from those of GCVE coils; also, the difference of the organs and tissues surrounding the metal may cause differences in CT value distribution around the metal. To the best of our knowledge, there have been no published reports regarding the effectiveness of spectral CT mono-energy image data collection combined with metal artifact reduction software (MARs) in reducing metal artifacts from GCVE coils by phantom experiments. Our study aims to explore the value of mono-energy image data collection combined with MARs of spectral CT imaging in reducing metal implant artifacts by simulating the attenuation of different tissues around the GCVE coils by phantom experiments.

Methods

This research protocol was approved by our institutional review board, and informed consent was not required because this study was a phantom study without human involvement.

Phantom and solution preparation

A quantitative standard phantom made of epoxy resin with eight standard cylinders around the body phantom and one standard cylinder in the middle was used. To simulate the attenuation of different tissues of the human body, each of the 8 cylinders surrounding the body phantom was filled with 20 mL of iodine solution of different concentrations. The concentration of the iodine solution was 1.75 mgI/mL (CT value =69 HU), 3.5 mgI/mL (CT value =111 HU), 7.0 mgI/mL (CT value =177 HU), 10.5 mgI/mL (CT value =253 HU), 14.0 mgI/mL (CT value =330 HU), 17.5 mgI/mL (CT value =417 HU), 35.0 mgI/mL (CT value =767 HU), and 70.0 mgI/mL (CT value =1,422 HU), simulating CT values of the hepatic parenchyma, enhanced liver parenchyma in the arterial phase, enhanced hepatic parenchyma in the portal phase, enhanced abdominal aorta, enhanced hepatic portal vein, enhanced inferior vena cava, calcification and bone, respectively. Then, 20 mL of sodium chloride solution was injected into the middle cylinder, and an embolic coil of 8 mm in diameter was placed in it.

CT scanning and image reconstruction

Using the spectral CT scanner (Revolution, GE Healthcare, USA), the phantom study was divided according to the different scanning methods into groups A and B. A conventional CT scanning mode was performed in group A with the following parameters: collimation 256×0.625 mm, tube voltage 120 kVp, and automatic milliampere tube current. Gemstone spectral imaging (GSI) mode was performed in group B: collimation 128×0.625 mm, tube voltage 80 kVp/140 kVp instantaneous switching, mA mode of GSI assist. Images were reconstructed with and without MARs mode. The pitch was 0.992:1; FOV was 25 cm; the layer thickness and reconstruction interval were 2.5 mm; pre-iterative reconstruction was 40%.

A data file with the information on the conventional poly-energy CT images of group A and a data file with the information on the spectral CT images of group B were all transmitted to AW4.7 workstation (GE Healthcare, USA). The spectral data of group B were reconstructed into 11 sets of monochromatic energy images (MonoE) from 40–140 keV with 10 keV intervals by spectral analysis software (GSI viewer). Therefore, four kinds of images, namely, group A of conventional poly-energy images, group B of MonoE, 120 kVp-like + MARs, and MonoE + MARs images, were obtained (*Figures 1-4*).

Image analysis

Along the long axis of the embolic coil, the regions of interest (ROIs) were placed within the three adjacent levels with the worst metallic artifacts. Four ROIs far from the coil without artifacts were selected at the same level. The size of the ROI was determined by the range of high- and low-density artifacts. The ROI is in the medial part of artifacts, and the edge of ROI cannot exceed the artifact number. To avoid errors, we measured the CT values (Hounsfield unit) and standard deviation (SD) values of the three ROIs of the worst metallic artifacts, and the CT values and SD values of the four ROIs far away from the metallic artifacts (the reference region without artifacts). Then, the differentiation between the CT values of the worst artifacts

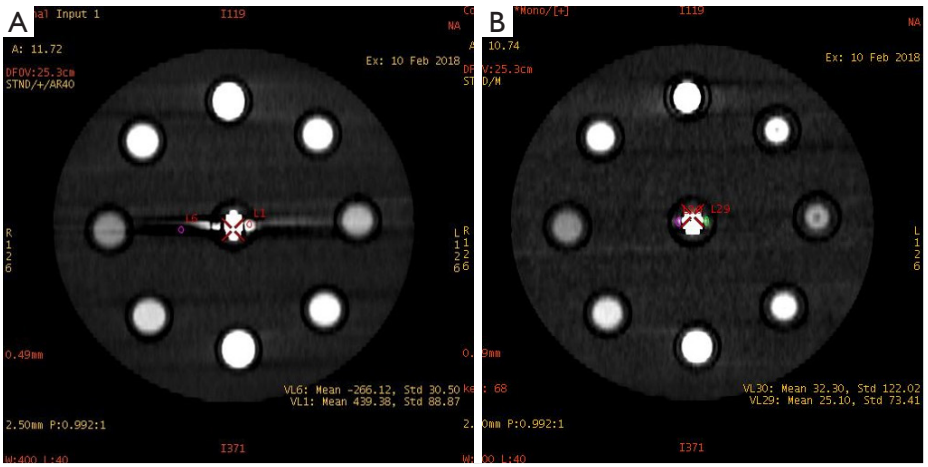

Figure 1 A comparison of high-attenuation artifacts and low-attenuation artifacts between the conventional poly-energy CT images (A) and 120 kVp-like + MARs images (B). Both the conventional poly-energy CT image (A) and the 120 kVp-like + MARs images (B) showed high- and low-attenuation stripe artifacts produced by the center spring coil, and the latter artifacts were significantly fewer than the former.

and the standard CT (the reference region without artifacts) values of the phantom were calculated. $\Delta CT = CT_{artifact} - CT_{standard}$. Artifact index (AI), $AI = \sqrt{SD1^2 - SD2^2}$, SD1 is the standard deviation in the worst artifacts, SD2 represents the standard deviation in the reference region without artifacts. The AI formula was introduced to quantify the severity of metal artifacts (15). Hardening artifacts removal rate (BAR), $BAR = (AI_{120kVp} - AI_{keV})/AI_{120kVp} \times 100\%$.

Statistical analysis

Statistical analysis was performed with the IBM SPSS Statistics 25.0 software. All numeric values were reported as the mean±SD. The analysis of variance (ANOVA) test was used to compare the values of ΔCT and AI of 120 kVp-like + MARs, MonoE, MonoE + MARs images with those of conventional poly-energy CT images. A paired *t*-test was used to compare the variation of the ΔCT values and AI values of MonoE and MonoE + MARs. Differences of P<0.05 were considered statistically significant.

Results

Comparisons of ΔCT values

The ΔCT values of the high-attenuation and low-attenuation artifacts in conventional poly-energy, 120 kVp-like + MARs, MonoE, and MonoE + MARs images are shown in *Table 1*. The ΔCT values of the high-attenuation artifacts were significantly lower in the 120 kVp-like + MARs, MonoE, and MonoE + MARs images than those in the conventional poly-energy CT images (P<0.05 for all). The ΔCT values of the low-attenuation artifacts were significantly lower in the 120 kVp-like + MARs and MonoE + MAR images than those in the conventional poly-energy CT images (P<0.05 for all). However, there were no significant differences between the MonoE images and the conventional CT images (P>0.05) (*Figure 5*).

Comparisons of AI values

The AI values of the high-attenuation and low-attenuation artifacts in the conventional poly-energy images, 120 kVp-like + MARs images, MonoE images, and MonoE + MARs images are shown in *Table 1*. The AI values of the high-attenuation artifacts decreased significantly in the 120 kVp-like + MARs, MonoE (110–140 keV), and MonoE + MARs images compared with the conventional poly-energy CT images (P<0.05 for all). However, there were no significant differences between the MonoE (40–100 keV) images and the conventional CT images (P>0.05). Compared with the conventional CT images, the AI values of the low-attenuation artifacts decreased significantly in the 120 kVp-like + MARs, MonoE (40–140 keV), and MonoE + MARs images (P<0.05 for all) (*Figure 6*).

Comparisons of BAR values

The BAR values of the high-attenuation and low-

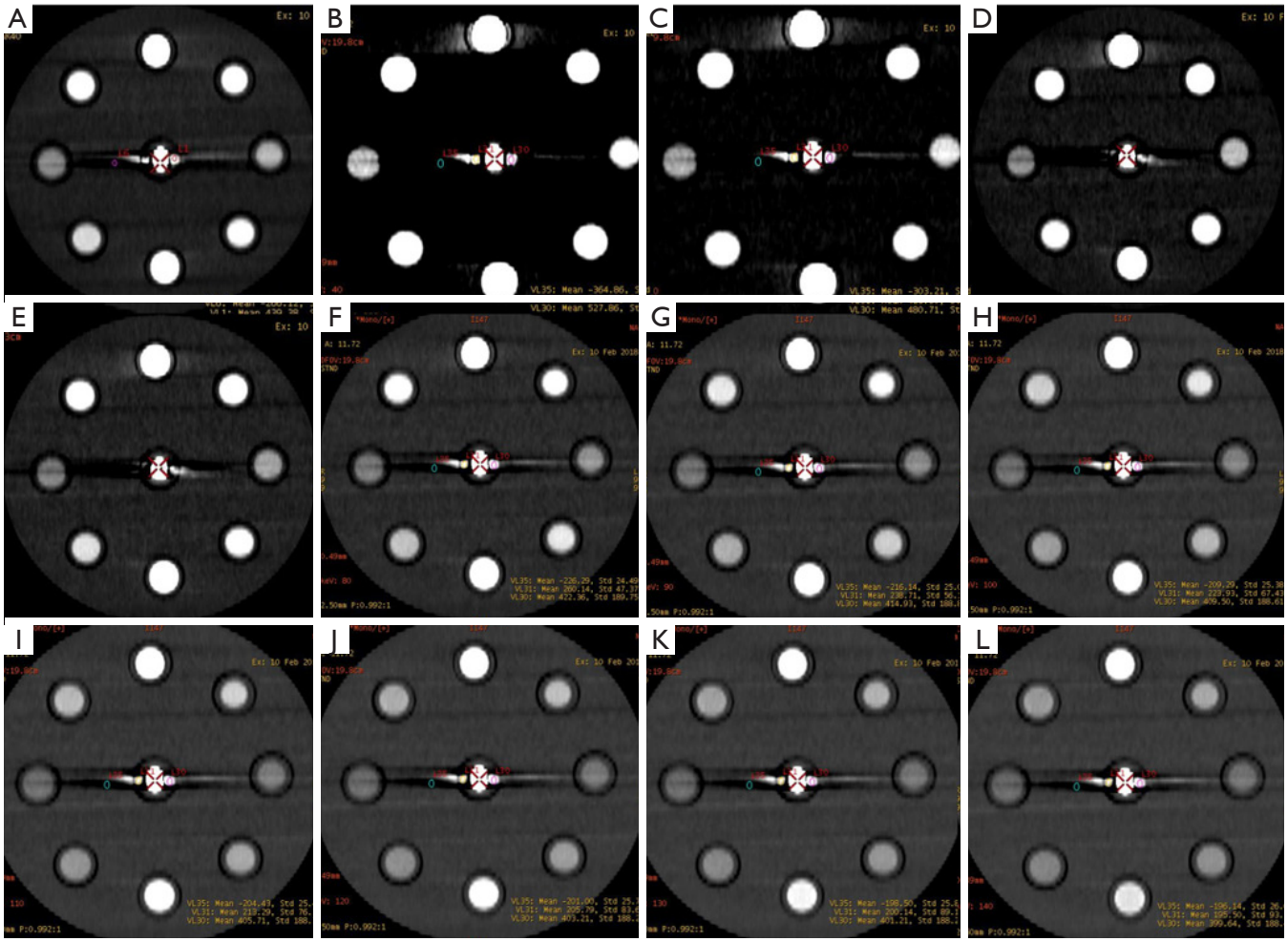

Figure 2 A comparison of high-attenuation artifacts and low-attenuation artifacts between a conventional poly-energy CT image (A) and 40–140 keV MonoE images (B,C,D,E,F,G,H,I,J,K,L). Both the conventional poly-energy CT image and the 40–140 keV MonoE images showed high- and low-attenuation stripe artifacts produced by the center spring coil, and the artifacts of the 110–140 keV MonoE images were fewer than those of conventional poly-energy CT images.

attenuation artifacts in conventional poly-energy images, 120 kVp-like + MARs images, MonoE images, and MonoE + MARs images are shown in *Table 1*. The BAR values of the high-attenuation and low-attenuation artifacts in the 120 kVp-like + MARs images were 82% and 92%, respectively. For the BAR values of the high-attenuation and low-attenuation artifacts in the MonoE and MonoE + MARs images, the maximum BAR values in the MonoE images at 120 keV MonoE level were 36% and 39%, respectively. Meanwhile, the maximum BAR values obtained at the 140 keV MonoE level in the MonoE + MARs images were 89% and 94%, respectively. In summary, the hardening artifact removal rates for both the high-attenuation and low-attenuation artifacts were highest in the MonoE + MARs images (*Figure 7*).

Discussion

Metal implants cause high attenuation when X-rays pass through as they are high atomic number materials, which results in projection data loss (16). Therefore, metal artifacts appear in CT image reconstruction. Metal artifacts are manifested in CT images as high attenuation and low attenuation stripe artifacts in the metal implant areas (17,18). However, due to the scattering of the physical properties (high attenuation and effective atomic number) of metal

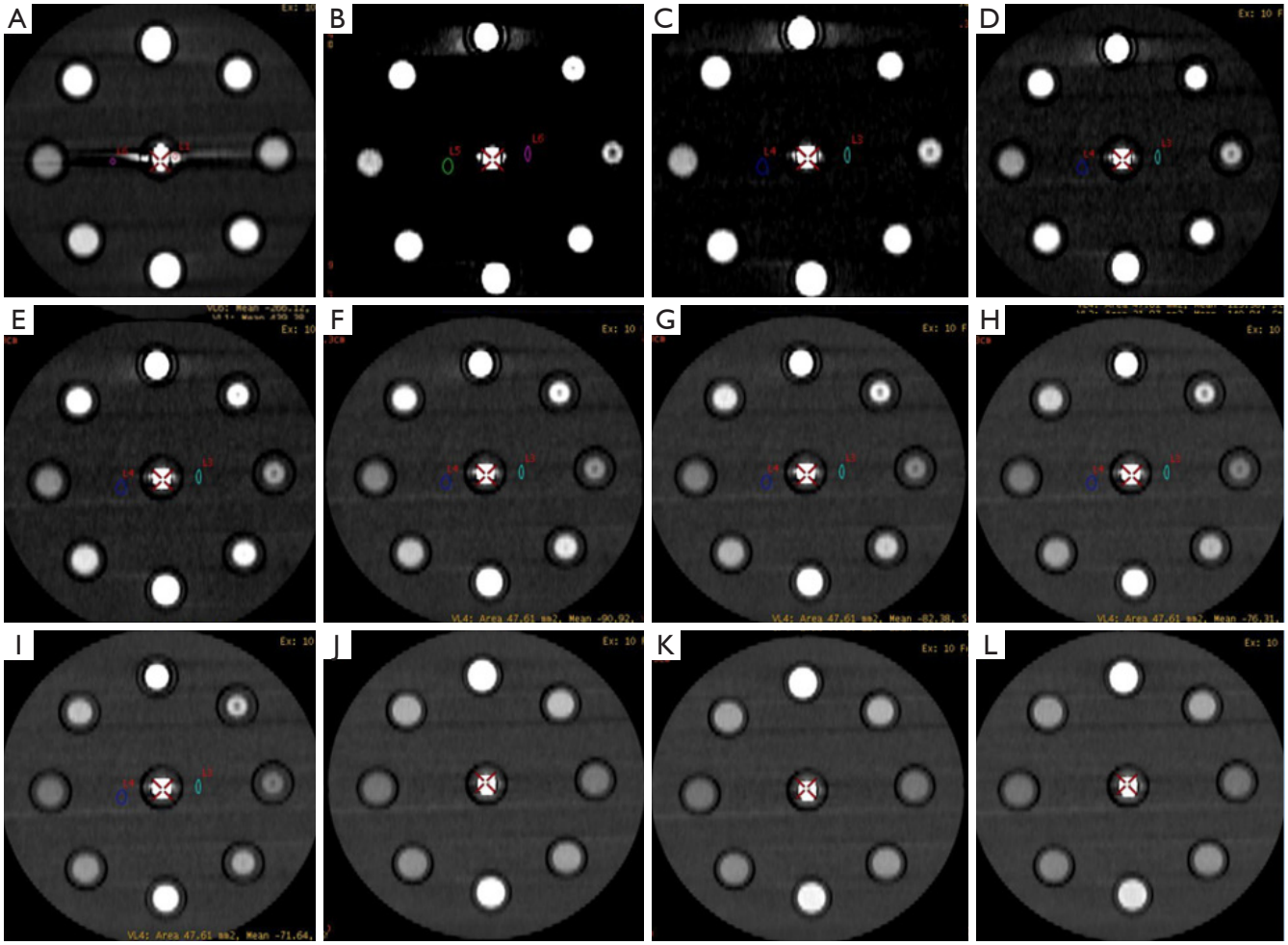

Figure 3 A comparison of high-attenuation artifacts and low-attenuation artifacts between a conventional poly-energy CT image (A) and 40–140 keV MonoE + MARs images (B,C,D,E,F,G,H,I,J,K,L). Both the conventional poly-energy CT image (A) and the 40–140 keV MonoE + MARs images (B,C,D,E,F,G,H,I,J,K,L) showed high- and low-attenuation stripe artifacts produced by the center spring coil, and the artifacts of the 40–140 keV MonoE + MARs images were fewer than those of conventional poly-energy CT images.

implants, higher image noise will also be present (3-6).

Early researchers believed that many methods could be used to correct the appearance of metal artifacts, including the interpolation of projections, Kalender's linear interpolation, and Zhao's linear interpolation of wavelet coefficients (11,19). Recently, image reconstruction using iterative reconstruction algorithms, including iterative reconstruction methods and local iterative poly-energy algorithms, could also be used to correct metal artifacts. Some studies have shown that the reconstruction of MonoE images by spectral CT can reduce metal artifacts (20-23). The spectral CT detection system uses a single X-ray source, which can obtain alternating high- and low-energy X-ray spectroscopy via rapid kVp switching (80 and 140 kVp). Using projection data acquired by two different energies, a synthetic MonoE image is generated. These virtual MonoE images can reduce beam hardening artifacts (24).

In our study, the ΔCT values of high attenuation artifacts in the 40–140 keV MonoE images were all decreased significantly ($P<0.05$) compared with conventional poly-energy CT images, but there were no significant differences in the ΔCT values of the low attenuation artifacts ($P>0.05$). In the 110–140 keV MonoE images, the high-attenuation artifact AI values were reduced. The AI values of the low-attenuation artifacts were decreased in the 40–140 keV MonoE images. Therefore, our study showed that 110–140 keV MonoE images had advantages in reducing high attenuation fringe artifacts caused by beam hardening.

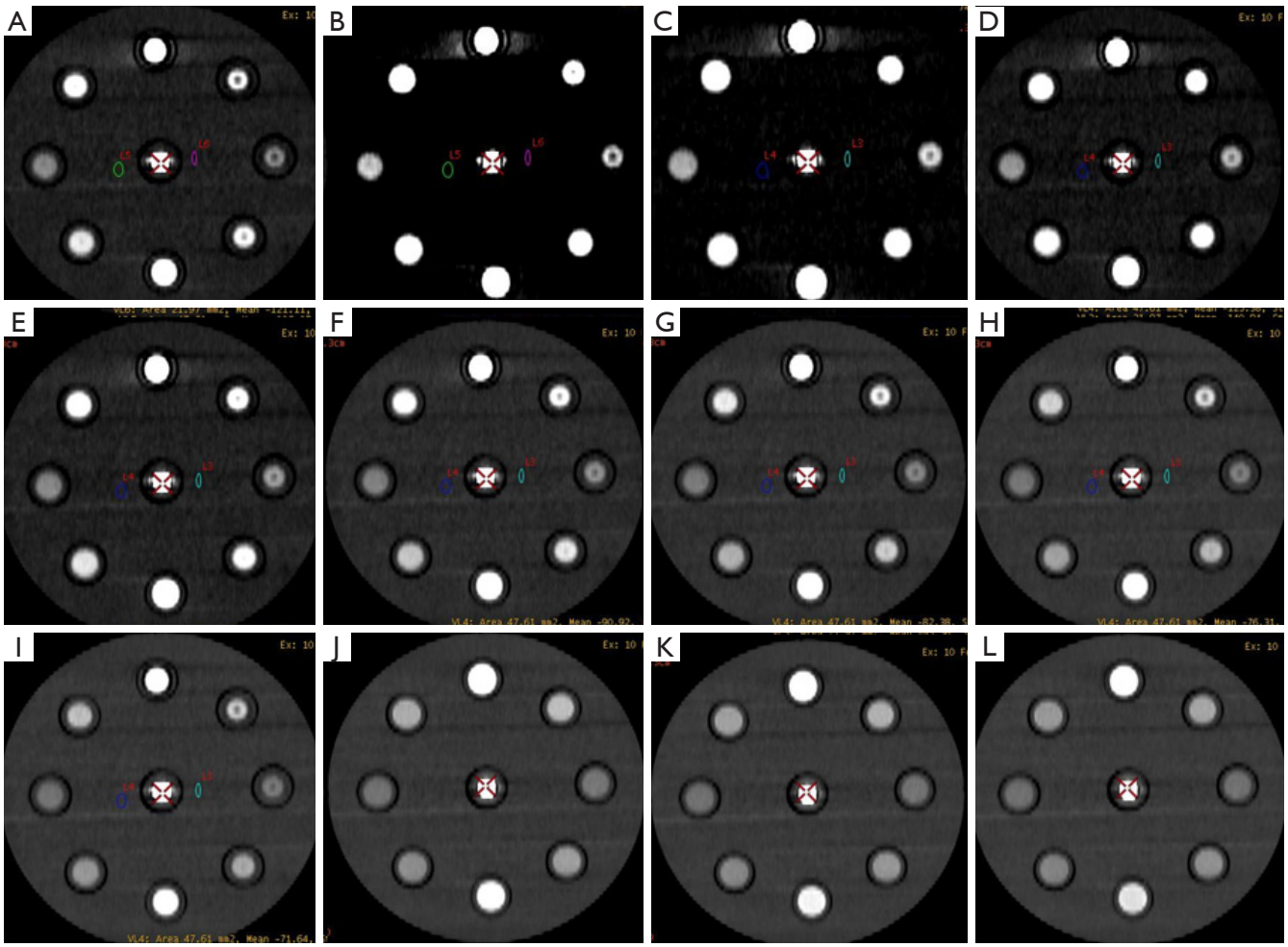

Figure 4 A comparison of high-attenuation artifacts and low-attenuation artifacts between a 120 kVp-like + MARs image (A) and 40–140 keV MonoE + MARs images (B,C,D,E,F,G,H,I,J,K,L). The 120 kVp-like + MARs image (A) and the 40–140 keV MonoE + MARs images (B,C,D,E,F,G,H,I,J,K,L) showed high- and low-attenuation stripe artifacts produced by the center spring coil, and the artifacts of the 70–140 keV MonoE + MARs images were fewer than those of MARs images.

MARs is a commercial product that implements an iterative reconstruction algorithm to mitigate the artifacts caused by metal objects in CT images. This method modifies the data destroyed by striped artifacts with undistorted projection data recognition by iterative reconstruction algorithm, thus reducing the metal artifacts (25,26). The combination of MARs and MonoE images is especially effective for solving low-attenuation fringe artifacts caused by photon starvation. Some researchers believe that, in theory, using MonoE images could reduce the beam hardening artifacts, and the artifacts could be reduced with the combined application of MARs further (22,25,27). In our study, conventional poly-energy CT images, 120 kVp-like + MARs, MonoE, and MonoE + MARs were compared and analyzed. The artifact index and hardening artifact removal rates were measured. The results showed that the ΔCT values and artifact index rate of the MonoE + MARs images were closer to the expected value than those of the MonoE images.

Furthermore, the differences between the two groups were statistically significant ($P<0.05$). Thus, compared with conventional poly-energy CT images and 110–140 keV MonoE images, the reconstruction images of MonoE + MARs can significantly reduce metal artifacts. As well as reducing the high-attenuation fringe artifacts caused by beam hardening, the MonoE + MARs method can also reduce the low-attenuation fringe artifacts caused by photon starvation. Specifically, the MonoE + MARs method can

Table 1 A comparison of the CT, AI, and BAR values of high-attenuation and low-attenuation artifacts in conventional poly-energy images, 120 kVp-like + MARs images, MonoE images, and MonoE + MARs images

Group	ΔCT value (HU)				AI value				BAR (%)	
	High density artifacts	Low density artifacts	High density artifacts P value	Low density artifacts P value	High density artifacts	Low density artifacts	High density artifacts P value	Low density artifacts P value	High density artifacts	Low density artifacts
Conventional CT scan	178.74±32.81	−112.67±32.88	–	–	36.97	37.05	–	–	–	–
120 kVp-like + MARs image	4.29±3.44	−1.50±0.92	<0.05	<0.05	6.65	3.07	<0.05	<0.05	82.02	91.70
40 keV + MARs	8.14±12.76	−2.69±1.88	<0.05	<0.05	20.84	6.59	<0.05	<0.05	43.63	82.20
50 keV + MARs	3.49±6.29	−1.50±0.92	<0.05	<0.05	11.55	4.64	<0.05	<0.05	68.77	87.47
60 keV + MARs	0.82±6.26	−1.76±1.03	<0.05	<0.05	10.49	3.57	<0.05	<0.05	71.63	90.36
70 keV + MARs	0.50±2.65	−1.48±0.77	<0.05	<0.05	5.61	2.77	<0.05	<0.05	84.83	92.51
80 keV + MARs	0.66±2.22	−1.30±0.79	<0.05	<0.05	4.73	2.61	<0.05	<0.05	87.21	92.96
90 keV + MARs	0.50±2.28	−1.13±0.82	<0.05	<0.05	4.51	2.47	<0.05	<0.05	87.80	93.33
100 keV + MARs	0.61±2.11	−1.00±0.87	<0.05	<0.05	4.24	2.51	<0.05	<0.05	88.54	93.21
110 keV + MARs	0.35±2.00	−1.06±0.96	<0.05	<0.05	4.01	2.59	<0.05	<0.05	89.15	93.01
120 keV + MARs	0.56±2.17	−1.11±0.66	<0.05	<0.05	4.12	2.05	<0.05	<0.05	88.85	94.47
130 keV + MARs	0.66±2.00	−1.05±0.80	<0.05	<0.05	3.91	2.27	<0.05	<0.05	89.41	93.86
140 keV + MARs	0.60±2.12	−1.06±0.81	<0.05	<0.05	3.94	2.22	<0.05	<0.05	89.34	94.02
40 keV	152.33±53.48	−76.71±19.65	<0.05	>0.05	63.48	28.57	>0.05	<0.05	−71.72	22.89
50 keV	130.96±31.33	−75.50±18.16	<0.05	>0.05	38.16	24.60	>0.05	<0.05	−3.23	33.59
60 keV	117.96±25.81	−74.50±18.14	<0.05	>0.05	31.14	23.29	>0.05	<0.05	15.78	37.12
70 keV	109.71±25.76	−74.13±18.60	<0.05	>0.05	30.01	22.74	>0.05	<0.05	18.83	38.62
80 keV	104.25±26.27	−73.92±19.18	<0.05	>0.05	29.98	22.81	>0.05	<0.05	18.91	38.44
90 keV	100.96±26.16	−73.55±19.51	<0.05	>0.05	29.33	22.63	>0.05	<0.05	20.66	38.92
100 keV	98.83±25.03	−73.25±19.57	<0.05	>0.05	28.04	22.54	>0.05	<0.05	24.15	39.17
110 keV	96.71±23.23	−73.46±19.97	<0.05	>0.05	25.97	22.68	<0.05	<0.05	29.76	38.77
120 keV	95.79±21.10	−73.17±19.94	<0.05	>0.05	23.58	22.41	<0.05	<0.05	36.22	39.50
130 keV	94.87±22.00	−73.13±20.05	<0.05	>0.05	24.51	22.55	<0.05	<0.05	33.71	39.13
140 keV	94.38±21.87	−73.00±20.35	<0.05	>0.05	24.13	22.61	<0.05	<0.05	34.72	38.97

$\Delta CT = CT_{artifact} - CT_{standard}$; AI, Artifact index; BAR, hardening artifacts removal rate.

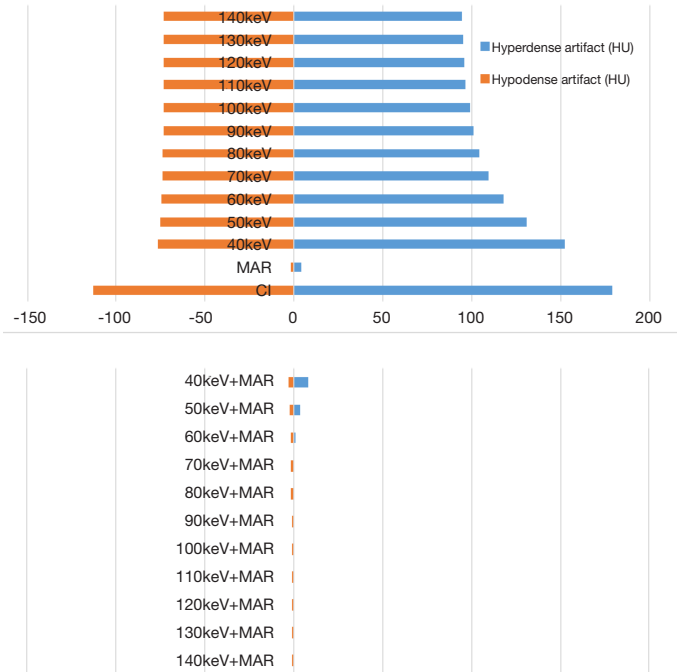

Figure 5 The ΔCT values of conventional poly-energy CT image, 120 kVp-like + MARs image, 40–140 keV MonoE images, and 40–140 keV MonoE + MARs images. Blue bands denote high-attenuation artifacts, and red bands denote low-attenuation artifacts. The ΔCT values of high- and low-attenuation artifacts in the MonoE and MonoE + MARs images decreased as the energy level increased. The ΔCT values of the high- and low-attenuation artifacts in the 120 kVp-like + MARs, MonoE, and MonoE + MARs images were lower than those of the conventional poly-energy CT images.

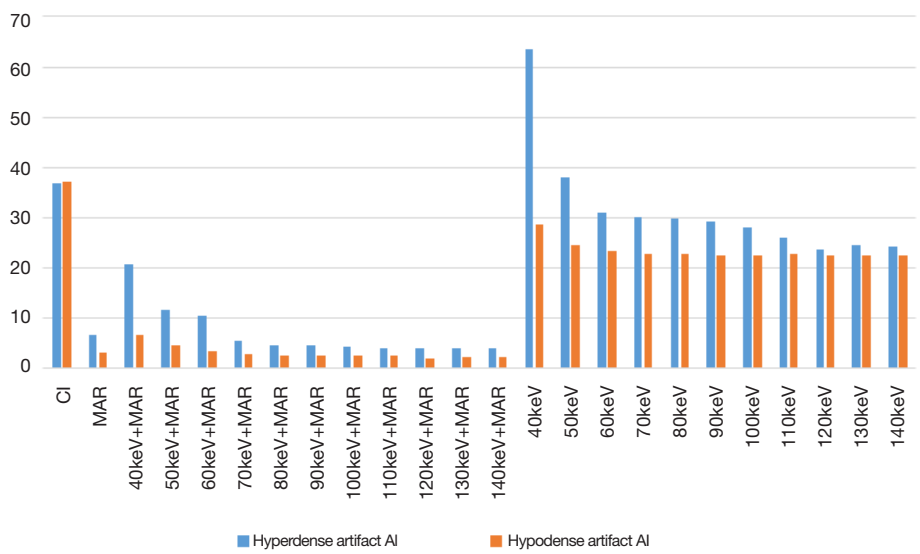

Figure 6 The AI values of the conventional poly-energy CT, 120 kVp-like + MARs, 40–140 keV MonoE, and 40–140 keV MonoE + MARs images. Blue bands denote high-attenuation artifacts, and red bands denote low-attenuation artifacts. The AI values of high- and low-attenuation artifacts in the MonoE and MonoE + MARs images decreased as the energy level increased. The AI values of the high- and low-attenuation artifacts in the 40–50 keV MonoE images were higher than that of the conventional poly-energy CT images.

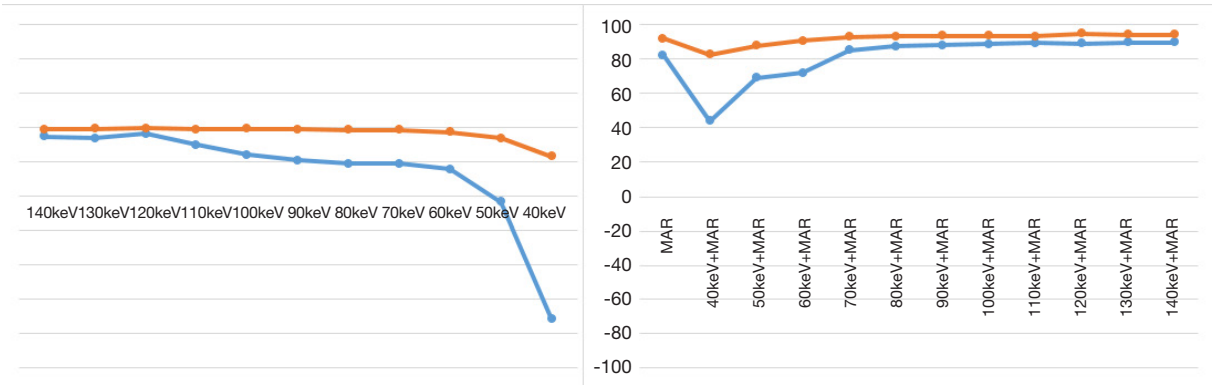

Figure 7 The BAR values of 120 kVp-like + MARs, 40–140 keV MonoE, and 40–140 keV MonoE + MARs images. Blue bands denote high-attenuation artifacts, and red bands denote low-attenuation artifacts. The BAR values of the high- and low-attenuation artifacts in the MonoE and MonoE + MARs images increased with the energy level. The BAR values of the high- and low-attenuation artifacts in the 120 kVp-like + MARs and MonoE + MARs images were higher than those of the MonoE images.

reduce the artifacts of metal implants further than only just using the MonoE and MARs method. Our results showed that 140 keV was an optimal level for MonoE image creation for metal artifact reduction with MARs.

This study has a number of limitations. First, the material used in this study was only an embolic coil; other types and materials implants were not included. Second, this study was a quantitative study of the phantom, and the effects of high- and low-attenuation artifacts produced by the coils on the surrounding tissues and organs *in vivo* were not evaluated. There was no subjective evaluation in the phantom study; therefore, future clinical research should use both observer (subjective) assessment and quantitative (objective) evaluation. Third, due to the limitations of the phantom conditions, the position of tissue cannot be simulated, so the influence of different attenuation tissue on artifacts was not evaluated, causing this also to be a limitation.

In conclusion, this study suggested that these three different reconstruction methods (120 kVp-like + MARs, 110–140 keV MonoE, and MonoE + MARs), compared with conventional poly-energy CT images, can reduce metal artifacts to varying degrees. Furthermore, MARs combined with the MonoE method has the greatest effect in reducing metal artifacts of high- and low-attenuation.

Acknowledgments

Funding: This study was supported by the National Natural Science Foundation of China (grant No. 61876216) and Beijing Shijitan Hospital, Capital Medical University (grant No. 2018-q01).

Footnote

Conflicts of Interest: All authors have completed the ICMJE uniform disclosure form (available at http://dx.doi.org/10.21037/qims-19-936). The authors have no conflicts of interest to declare.

Ethical Statement: This research protocol was approved by our institutional review board, and informed consent was not required because this study was a phantom study without human involvement.

References

1. Wan YM, Li YH, Xu Y, Wu HM, Li YC, Wu XN, Yang JH. Predictors of Shunt Dysfunction and Overall Survival in Patients with Variceal Bleeding Treated with

Transjugular Portosystemic Shunt Creation Using the Fluency Stent Graft. Acad Radiol 2018;25:925-34.
2. Moulin B, Chevallier O, Abdulmalak G, Luu M, Latournerie M, Minello A, Gehin S, Cercueil JP, Midulla M. Loffroy R. Persistence of gastric or esophageal varices on final angiography increases transjugular intrahepatic portosystemic shunt revision rate after polytetrafluoroethylene-covered stent shunt creation. Quant Imaging Med Surg 2018;8:174-81.
3. Große Hokamp N, Neuhaus V, Abdullayev N, Laukamp K, Lennartz S, Mpotsaris A, Borggrefe J. Reduction of artifacts caused by orthopedic hardware in the spine in spectral detector CT examinations using virtual monoenergetic image reconstructions and metal-artifact-reduction algorithms. Skeletal Radiol 2018;47:195-201.
4. Mori I, Machida Y, Osanai M, Iinuma K. Photon starvation artifacts of X-ray CT: their true cause and a solution. Radiol Phys Technol 2013;6:130-41.
5. Kalisz K, Buethe J, Saboo SS, Abbara S, Halliburton S, Rajiah P. Artifacts at Cardiac CT: Physics and Solutions. Radiographics 2016;36:2064-83.
6. Bushberg JT. The AAPM/RSNA physics tutorial for residents: X-ray interactions. Radiographics 1998;18:457-68.
7. Bamberg F, Dierks A, Nikolaou K, Reiser MF, Becker CR, Johnson TRC. Metal artifact reduction by dual energy computed tomography using monoenergetic extrapolation. Eur Radiol 2011;21:1424-9.
8. Mahnken AH, Raupach R, Wildberger JE, Jung B, Heussen N, Flohr TG, Günther RW, Schaller S. A new algorithm for metal artifact reduction in computed tomography: in vitro and in vivo evaluation after total hip replacement. Invest Radiol 2003;38:769-75.
9. Glover GH, Pelc NJ. An algorithm for the reduction of metal clip artifacts in CT reconstructions. Med Phys 1981;8:799-807.
10. Große Hokamp N, Eck B, Siedek F, Pinto Dos Santos D, Holz JA, Maintz D, Haneder S. Quantification of metal artifacts in computed tomography: methodological considerations. Quant Imaging Med Surg 2020;10:1033-44.
11. Kalender WA, Hebel R, Ebersberger J. Reduction of CT artifacts caused by metallic implants. Radiology 1987;164:576-7.
12. Kim YJ, Cha JG, Kim H, Yi JS, Kim HJ. Dual-Energy and Iterative Metal Artifact Reduction for Reducing Artifacts Due to Metallic Hardware: A Loosening Hip Phantom Study. AJR Am J Roentgenol 2019. doi: 10.2214/AJR.18.20413.
13. Neuhaus V, Grosse Hokamp N, Zopfs D, Laukamp K, Lennartz S, Abdullayev N, Maintz D, Borggrefe J. Reducing artifacts from total hip replacements in dual layer detector CT: Combination of virtual monoenergetic images and orthopedic metal artifact reduction. Eur J Radiol 2019:14-20.
14. Winklhofer S, Hinzpeter R, Stocker D, Baltsavias G, Michels L, Burkhardt JK, Regli L, Valavanis A, Alkadhi H. Combining monoenergetic extrapolations from dual-energy CT with iterative reconstructions: reduction of coil and clip artifacts from intracranial aneurysm therapy. Neuroradiology 2018;60:281-91.
15. Wang Y, Qian B, Li B, Qin G, Zhou Z, Qiu Y, Sun X, Zhu B. Metal artifacts reduction using monochromatic images from spectral CT: evaluation of pedicle screws in patients with scoliosis. Eur J Radiol 2013;82:e360-6.
16. Lee MJ, Kim S, Lee SA, Song HT, Huh YM, Kim DH, Han SH, Suh JS. Overcoming artifacts from metallic orthopedic implants at high-field-strength MR imaging and multi-detector CT. Radiographics 2007;27:791-803.
17. Andersson KM, Nowik P, Persliden J, Thunberg P, Norrman E. Metal artefact reduction in CT imaging of hip prostheses—an evaluation of commercial techniques provided by four vendors. Br J Radiol 2015;88:20140473.
18. Stradiotti P, Curti A, Castellazzi G, Zerbi A. Metal-related artifacts in instrumented spine. Techniques for reducing artifacts in CT and MRI: state of the art. Eur Spine J 2009;18 Suppl 1:102-8.
19. Zhao S, Robertson DD, Wang G, Whiting B, Bae KT. X-ray CT metal artifact reduction using wavelets: an application for imaging total hip prostheses. IEEE Trans Med Imaging 2000;19:1238-47.
20. Wellenberg RHH, Hakvoort ET, Slump CH, Boomsma MF, Maas M, Streekstra GJ. Metal artifact reduction techniques in musculoskeletal CT-imaging. Eur J Radiol 2018;107:60-9.
21. Katsura M, Sato J, Akahane M, Kunimatsu A, Abe O. Current and Novel Techniques for Metal Artifact Reduction at CT: Practical Guide for Radiologists. Radiographics 2018;38:450-61.
22. Pessis E, Sverzut JM, Campagna R, Guerini H, Feydy A, Drapé JL. Reduction of Metal Artifact with Dual-Energy CT: Virtual Monospectral Imaging with Fast Kilovoltage Switching and Metal Artifact Reduction Software. Semin Musculoskelet Radiol 2015;19:446-55.
23. Pessis E, Campagna R, Sverzut JM, Bach F, Rodallec M, Guerini H, Feydy A, Drapé JL. Virtual monochromatic spectral imaging with fast kilovoltage switching: reduction

of metal artifacts at CT. Radiographics 2013;33:573-83.
24. Huang JY, Kerns JR, Nute JL, Liu X, Balter PA, Stingo FC, Followill DS, Mirkovic D, Howell RM, Kry SF. An evaluation of three commercially available metal artifact reduction methods for CT imaging. Phys Med Biol 2015;60:1047-67.
25. Kidoh M, Nakaura T, Nakamura S, Tokuyasu S, Osakabe H, Harada K, Yamashita Y. Reduction of dental metallic artifacts in CT: value of a newly developed algorithm for metal artefact reduction (O-MAR). Clin Radiol 2014;69:e11-16.
26. Li H, Noel C, Chen H, Harold Li H, Low D, Moore K, Klahr P, Michalski J, Gay HA, Thorstad W, Mutic S. Clinical evaluation of a commercial orthopedic metal artifact reduction tool for CT simulations in radiation therapy. Med Phys 2012;39:7507-17.
27. Lee YH, Park KK, Song HT, Kim S, Suh JS. Metal artefact reduction in gemstone spectral imaging dual-energy CT with and without metal artefact reduction software. Eur Radiol 2012;22:1331-40.

Cite this article as: Sun X, Zhao Q, Sun P, Yao Z, Wang R. Metal artifact reduction using mono-energy images combined with metal artifact reduction software in spectral computed tomography: a study on phantoms. Quant Imaging Med Surg 2020;10(7):1515-1525. doi: 10.21037/qims-19-936

